

## Extended-localized transition in diffusive quasicrystals

Zhoufei Liu<sup>1</sup>, Pei-Chao Cao,<sup>2,3,4</sup> Ying Li,<sup>2,3,4,\*</sup> and Jiping Huang<sup>1,†</sup>

<sup>1</sup>*Department of Physics, State Key Laboratory of Surface Physics, and Key Laboratory of Micro and Nano Photonic Structures (Ministry of Education), Fudan University, 200438 Shanghai, China*

<sup>2</sup>*State Key Laboratory of Extreme Photonics and Instrumentation, ZJU-Hangzhou Global Scientific and Technological Innovation Center, Zhejiang University, Hangzhou, 310027 Zhejiang, China*

<sup>3</sup>*International Joint Innovation Center, Key Laboratory of Advanced Micro/Nano Electronic Devices and Smart Systems of Zhejiang, The Electromagnetics Academy of Zhejiang University, Zhejiang University, Haining, 314400 Zhejiang, China*

<sup>4</sup>*Shaoxing Institute of Zhejiang University, Zhejiang University, Shaoxing, 312000 Zhejiang, China*



(Received 7 August 2023; revised 6 March 2024; accepted 24 May 2024; published 14 June 2024)

Compared with periodic systems, quasicrystals without translational invariance exhibit unexpected localization properties. The extended-localized transition in quasicrystals has been observed in both quantum and classical wave systems. However, its manifestation in diffusion systems, which serve as novel platforms for exploring phases of matter in condensed-matter physics, remains unexplored. Here we present an implementation of the extended-localized transition in a diffusive quasicrystal based on a coupled-ring chain structure. By modulating the thermal conductivities of the rings, we obtain the diffusive one-dimensional Aubry-André-Harper (AAH) model, which exhibits an extended-localized transition. Thanks to the ring-shaped chain, we clearly demonstrate the extended-localized transition under uniform excitation through temperature-field simulations. For the localized state, the temperature field clearly demonstrates a phenomenon of multiple localization centers, which has no counterpart in wave systems. We also quantitatively investigate the temperature evolution and size effect of this transition. Furthermore, local excitation is used to demonstrate the temperature field for both the extended state and the localized state. Besides, we implement the non-Hermitian diffusive AAH model by rotating the rings, whose temperature field shows a phenomenon of moving multiple localization centers in the localized phase. Finally, we give experimental suggestions for the diffusive AAH model and propose a potential application named the “double-trace distributed generator.” Our results should facilitate the design of flexible thermal devices and efficient heat management.

DOI: 10.1103/PhysRevApplied.21.064035

### I. INTRODUCTION

Anderson localization is an old but still-important research topic in condensed-matter physics [1]. A common belief is that any infinitesimal disorder leads to the localization of all eigenstates in one-dimensional systems without the extended-localized transition [2,3]. However, it has been discovered that the extended-localized transition can occur in quasiperiodic systems at a finite transition point, such as the Aubry-André-Harper (AAH) model [4,5]. The prototypical AAH model has been experimentally realized in both quantum [6–8] and classical [9–12] wave systems. Besides, there has been a great deal of interest in studying the extended-localized transition of the non-Hermitian AAH model recently [13–18], which presents new opportunities for quasicrystals.

Diffusion systems, inherently dissipative in nature, play a critical role in heat and mass transfer. Thermal metamaterials [19–23] enable diverse and flexible manipulation of heat flow, including cloaking [24–28], illusion [29–34], and chameleonlike behaviors [35,36]. Recently, topological phases of matter and non-Hermitian physics have been realized in diffusion systems [37], such as the exceptional point [38–40], the Weyl exceptional ring [41], the robust edge state [42], the one-dimensional Su-Schrieffer-Heeger model [43–45], a higher-order topological insulator [46–48], and the non-Hermitian skin effect [49–52]. Diffusion systems are widely regarded as excellent platforms for exploring novel phases in condensed-matter physics.

However, the quasiperiodic extended-localized transition has not yet been observed in diffusion systems. The primary challenge lies in the nonlocal evolution for excitations commonly used in naturally dissipative diffusion systems. While previous studies have worked with diffusive localized states (i.e., topological edge modes) [42,44,45],

\*Corresponding author: eleying@zju.edu.cn

†Corresponding author: jphuang@fudan.edu.cn

these modes decay rapidly without a clear observation in the temperature field. Moreover, the observation of these localized states necessitates specific initial conditions to align the temperature evolution with their decay rates, further complicating their study. Thus, uncovering diffusive localized states is a highly inconvenient yet crucial task.

In this paper, we propose an extended-localized transition based on a diffusive quasicrystal. The diffusive AAH model is constructed by the coupled-ring chain structure. By modulating the thermal conductivities of the rings, we obtain the diffusive counterpart of AAH model, which exhibits both diffusive extended and localized states. Through temperature-field simulations, we clearly illustrate the extended-localized transition under uniform excitation. Specifically, the temperature field corresponding to the diffusive localized state exhibits a phenomenon of multiple localization centers, which is unique in diffusion systems without the wave counterpart. A quantitative analysis of this transition is performed by our investigating the temperature evolution and size effect. Besides, we change the initial condition as the local excitation to show both the extended state and the localized state. Furthermore, we introduce anti-parity-time (APT) symmetry into the diffusive AAH model. This non-Hermitian model demonstrates a phenomenon of moving multiple localization centers in the localized phase. Finally, we provide experimental suggestions for the diffusive AAH model and present a potential application dubbed the “double-trace distributed generator.” Our work offers insights into efficient and robust heat manipulation and provides a distinct mechanism of heat insulation.

The outline for the rest of this paper is as follows. In Sec. II, we introduce the coupled-ring chain structure and derive its effective Hamiltonian. In Sec. III, we obtain the diffusive AAH model by mapping the original AAH model onto the coupled-ring chain structure and discuss its properties. In Sec. IV, we report the temperature-field simulation of the extended-localized transition under uniform excitation. We also quantitatively investigate the temperature evolution and size effect of this transition. In Sec. V, we discuss the extended-localized transition under local excitation. In Sec. VI, we implement the diffusive APT symmetric AAH model and report the temperature-field simulation. We give experimental suggestions in Sec. VII and propose a potential application in Sec. VIII. Finally, our conclusions are given in Sec. IX.

## II. COUPLED-RING CHAIN STRUCTURE

We start by considering the coupled-ring chain structure, as depicted in Fig. 1(a). The structure consists of several rings vertically coupled in the  $z$  direction to form a chain through interlayers. We denote the interior and exterior radii of the rings by  $R_1$  and  $R_2$ , respectively. For simplicity,

we assume that  $R_1 \approx R_2 \approx R$  and that the ring’s perimeter  $L = 2\pi R$ . The thickness of the ring and the thickness of the interlayer are denoted by  $b$  and  $d$ , respectively. Using Fourier’s law of heat conduction, we can write the thermal-coupling equation for the  $j$  th ring as

$$\begin{aligned} \frac{\partial T_j(x, t)}{\partial t} &= \frac{\kappa_j}{\rho_j C_j} \frac{\partial^2 T_j(x, t)}{\partial x^2} + v_j \frac{\partial T_j(x, t)}{\partial x} \\ &\quad + h_{j-1,j} [T_{j-1}(x, t) - T_j(x, t)] \\ &\quad + h_{j,j} [T_{j+1}(x, t) - T_j(x, t)], \end{aligned} \quad (1)$$

where  $T_j(x, t)$ ,  $v_j$ ,  $\kappa_j$ ,  $\rho_j$ , and  $C_j$  are the temperature field, rotation velocity, thermal conductivity, mass density, and heat capacity of the  $j$  th ring, respectively, and  $x$  is the position along the ring. The heat-exchange rate between the  $(j-1)$  th interlayer and the  $j$  th ring is denoted by  $h_{j-1,j} = \kappa_{1,j-1}/\rho_j C_j bd$ , where  $\kappa_{1,j-1}$  is the thermal conductivity of the  $(j-1)$  th interlayer. Similarly, the heat-exchange rate between the  $j$  th interlayer and the  $j$  th ring is denoted by  $h_{j,j} = \kappa_{1,j}/\rho_j C_j bd$ . As the temperature field of the ring is periodic, we can assume that Eq. (1) has a plane-wave solution of the form  $T_j(x, t) = A_j e^{i(\beta x - \omega t)}$ , where  $A_j$  is the amplitude of the temperature field of the  $j$  th ring and  $\omega$  is the decay rate. Here,  $\beta = 2m\pi/L = m/R$  is the propagation constant, where  $m$  is the mode order. In this study, we focus on the fundamental mode ( $m = 1$ ) because only the slowest-decaying mode can be clearly observed in diffusion systems. Substituting the plane-wave solution into Eq. (1), we obtain the effective Hamiltonian of the coupled-ring chain structure under the open boundary condition. The Hamiltonian can be written in the second-quantized form:

$$\hat{H} = i \sum_j \left[ h_{j,j+1} \hat{c}_{j+1}^\dagger \hat{c}_j + h_{j,j} \hat{c}_j^\dagger \hat{c}_{j+1} + (S_j + i\beta v_j) \hat{c}_j^\dagger \hat{c}_j \right], \quad (2)$$

where  $i = \sqrt{-1}$  denotes the imaginary unit, and  $\hat{c}_j^\dagger$  and  $\hat{c}_j$  are the creation and annihilation operators of the  $j$  th ring, respectively. The rotation term can be introduced to investigate the non-Hermitian effect in thermal diffusion, which corresponds to the gain and loss in wave systems [38]. The on-site term  $S_j$  takes the form of  $S_j = -(\beta^2 D_j + h_{j-1,j} + h_{j,j})$  in the bulk and  $S_{1(N)} = -(\beta^2 D_{1(N)} + h_{1,1(N-1,N)})$  at the boundary. Here,  $D_j = \kappa_j/\rho_j C_j$  represents the diffusivity of the  $j$  th ring. Furthermore,  $N$  denotes the total number of rings. This ring-shaped chain can help localize the temperature field and thus contribute to the implementation of the diffusive localized state.

## III. DIFFUSIVE AAH MODEL

We aim to obtain the anti-Hermitian diffusive AAH Hamiltonian by mapping the Hermitian AAH model onto

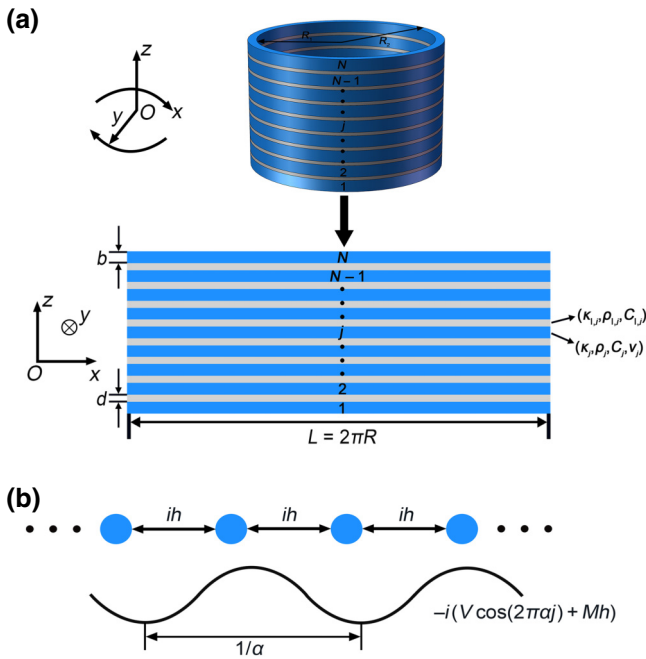


FIG. 1. Schematic diagram of diffusive AAH model. (a) Coupled-ring chain structure. The blue area denotes the ring, while the gray area represents the interlayer. The diagram is presented in three dimensions for clarity. To simplify the depiction, we have transformed the rings into planar channels and set the periodic boundary condition at both ends, as shown in the lower diagram. The bottom channel is denoted as the first ring, while the top channel is denoted as the  $N$  th ring. (b) Equivalent tight-binding model, with the on-site potential  $-i(V\cos(2\pi\alpha j) + Mh)$ .

the ring chain's Hamiltonian. The original AAH Hamiltonian is given by

$$\hat{H} = \sum_j [t\hat{c}_{j+1}^\dagger \hat{c}_j + t\hat{c}_j^\dagger \hat{c}_{j+1} + V\cos(2\pi\alpha j)\hat{c}_j^\dagger \hat{c}_j], \quad (3)$$

where  $t$  is the hopping amplitude,  $V$  is the strength of the quasiperiodic potential, and  $\alpha$  is an irrational number, usually chosen as the inverse golden ratio. To obtain the anti-Hermitian diffusive AAH Hamiltonian, we multiply the original Hamiltonian by  $i$  and replace  $t$  with the heat-exchange rate  $h$ . Additionally, we should add a constant term  $Mh$  to the on-site potential to ensure that the adjusted thermal conductivities of the rings are positive, where  $M$  is a constant. The effective diffusive AAH Hamiltonian can be written as

$$\hat{H} = i \sum_j \left[ h\hat{c}_{j+1}^\dagger \hat{c}_j + h\hat{c}_j^\dagger \hat{c}_{j+1} - (V\cos(2\pi\alpha j) + Mh)\hat{c}_j^\dagger \hat{c}_j \right], \quad (4)$$

where  $h = \kappa_1/\rho C b d$  is the heat-exchange rate. The equivalent tight-binding model is demonstrated in Fig. 1(b).

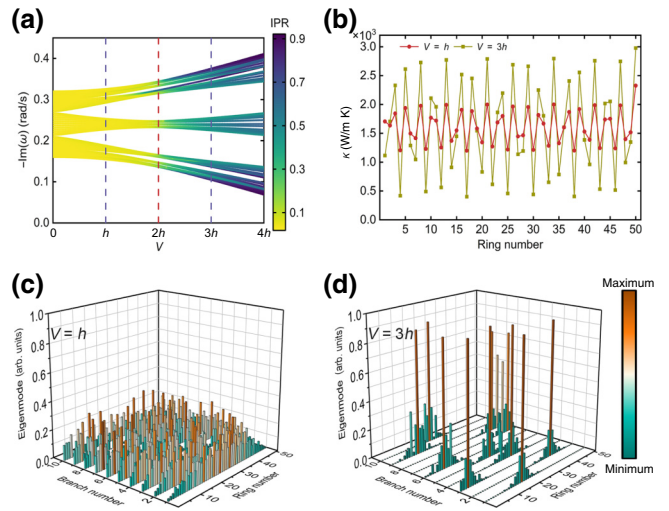


FIG. 2. Diffusive AAH model. (a) Decay rates with different strengths of the quasiperiodic potential. The color bar indicates the IPR. The dashed red line marks the extended-localized transition point  $V = 2h$ . (b) Adjusted thermal conductivities of each ring for the extended state ( $V = h$ ) and the localized state ( $V = 3h$ ), which are marked as dashed purple lines in (a). Eigenstate distributions of the ten slowest-decaying branches for (c) the extended state and (d) the localized state. The parameters are  $b = 12.5$  mm,  $d = 2$  mm,  $R = 100$  mm,  $\rho = 1000$  kg/m<sup>3</sup>,  $C = 1000$  J/kg K,  $\kappa_1 = 1$  W/m K,  $M = 6$ , and  $\alpha = (\sqrt{5} - 1)/2$ . The number of rings  $N$  is 50.

The decay rates with different strengths of the quasiperiodic potential are shown in Fig. 2(a). Here we use the inverse participation ratio (IPR) to characterize the degree of localization for each eigenstate [14,17,18]. The IPR is defined as  $\rho_{\text{IPR}} = \sum_j |\psi_j(E)|^4 / (\sum_j |\psi_j(E)|^2)^2$ , where  $\psi_j(E)$  is the  $j$  th component of the eigenstate corresponding to energy  $E$ . For an extended state,  $\rho_{\text{IPR}} \approx 1/N$  and approaches zero as  $N \rightarrow \infty$ . On the other hand,  $\rho_{\text{IPR}} \approx 1$  for a fully localized state. A clear extended-localized transition can be observed for each branch in the spectrum. The eigenstate distributions of the ten slowest-decaying branches for the extended state ( $V = h$ ) and the localized state ( $V = 3h$ ) are shown in Figs. 2(c) and 2(d). For the extended state, the eigenstates are almost evenly distributed, while for the localized state, each eigenstate is localized at a certain ring. Furthermore, the Lyapunov exponent is also an important quantity to characterize the localization. We have extracted the Lyapunov exponent of the diffusive AAH model from the theoretical and simulated eigenstate distributions, which is discussed in Appendix A. An obvious extended-localized transition can also be demonstrated in the Lyapunov exponent (see Fig. 8).

To meet the requirements of the AAH model, it is necessary to adjust the parameters of the rings and the interlayers. The velocities of the rings should be set to zero because

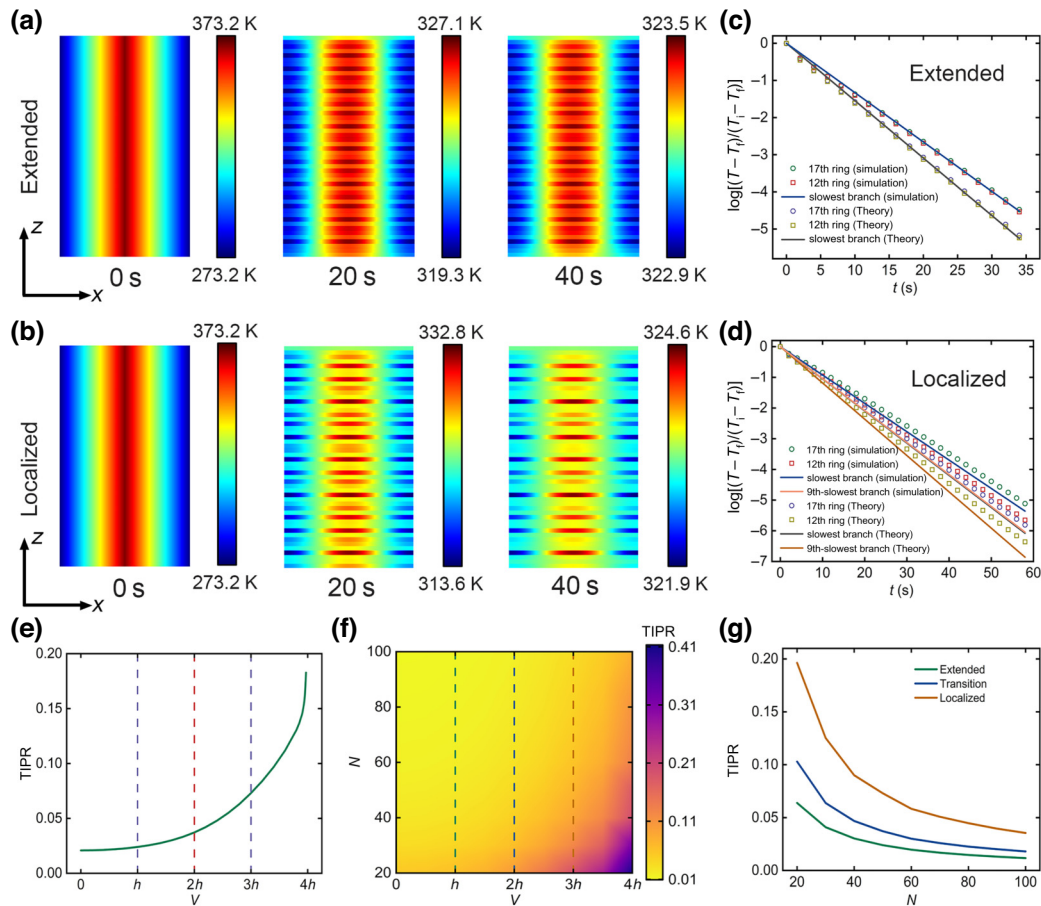


FIG. 3. Temperature-field simulations of the extended-localized transition under uniform excitation. (a) Extended state ( $V = h$ ) and (b) localized state ( $V = 3h$ ). (c) Simulated and theoretical normalized maximum-temperature evolutions of the 17th and 12th rings for the extended state. The blue and gray lines are the reference lines predicted by the simulated and theoretical decay rates of the slowest-decaying branch. (d) Simulated and theoretical normalized maximum-temperature evolutions of the 17th and 12th rings for the localized state. The blue and yellowish-pink lines are the reference lines predicted by the simulated decay rates of the slowest-decaying and ninth-slowest-decaying branches. The gray and brown lines are the reference lines predicted by the theoretical decay rates of the slowest-decaying and ninth-slowest-decaying branches. The number of rings  $N$  is 50. (e) TIPR with different strengths of the quasiperiodic potential. The temperature field used to calculate the TIPR is the final state (see Appendix B). (f) Phase diagram of the TIPR with different numbers of rings  $N$  and strengths of the quasiperiodic potential  $V$ . (g) TIPR with different numbers of rings for the extended state, the transition point, and the localized state, which are marked as dashed lines in (f). The highest and lowest temperatures in the temperature-field simulations are set as  $T_h = 373.2$  K and  $T_l = 273.2$  K. In the  $y$ -axis label in (c),(d),  $T_f = (T_h + T_l)/2 = 323.2$  K and  $T_i = T_h = 373.2$  K. The parameters are the same as in Fig. 2.

the diffusive AAH model is anti-Hermitian, which corresponds to the Hermitian AAH model in wave systems. The thermal conductivity of the ring is the only parameter that requires adjustment. By comparing the diffusive AAH Hamiltonian with the ring chain's Hamiltonian, one can observe the following correspondence:

$$\begin{aligned} S_1 &= -(\beta^2 D_1 + h) = -(V \cos(2\pi\alpha) + Mh), \\ S_j &= -(\beta^2 D_j + 2h) = -(V \cos(2\pi\alpha j) + Mh), \\ S_N &= -(\beta^2 D_N + h) = -(V \cos(2\pi\alpha N) + Mh), \end{aligned} \quad (5)$$

where  $j = 2, \dots, N - 1$ . By solving these equations, one can obtain the adjusted thermal conductivities of the rings.

We present two examples of adjusted thermal conductivities for the extended state ( $V = h$ ) and the localized state ( $V = 3h$ ) in Fig. 2(b).

#### IV. TEMPERATURE-FIELD SIMULATIONS OF THE DIFFUSIVE AAH MODEL UNDER UNIFORM EXCITATION

Next we perform temperature-field simulations to investigate the extended-localized transition. Firstly, we choose uniform excitation as the initial condition (see Appendix B). For the diffusive extended state at  $V = h$ , the temperature field is evenly distributed and concentrates

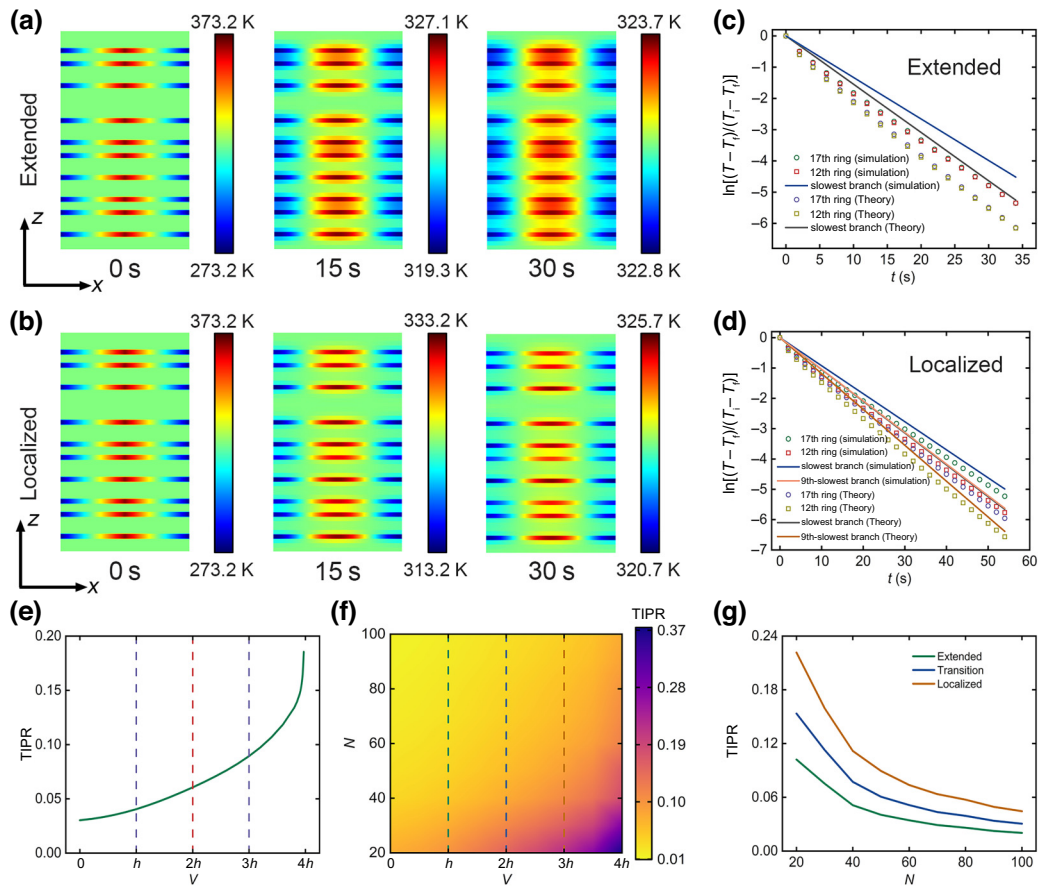


FIG. 4. Temperature-field simulations of the extended-localized transition under local excitation. (a) Extended state ( $V = h$ ) and (b) localized state ( $V = 3h$ ). (c) Simulated and theoretical normalized maximum-temperature evolutions of the 17th and 12th rings for the extended state. (d) Simulated and theoretical normalized maximum-temperature evolutions of the 17th and 12th rings for the localized state. (e) TIPR with different strengths of the quasiperiodic potential. (f) Phase diagram of the TIPR with different numbers of rings  $N$  and strengths of the quasiperiodic potential  $V$ . (g) TIPR with different numbers of rings for the extended state, the transition point, and the localized state, which are marked as dashed lines in (f). Other parameters are the same as in Fig. 3.

at the center, as depicted in Fig. 3(a), while for the diffusive localized state at  $V = 3h$ , as depicted in Fig. 3(b), the temperature distribution becomes highly localized with multiple distinct localization centers. This multiplicity comes from the closeness of the decay rates among several slowly decaying branches, and is distinct in diffusion systems without the wave counterpart. Consequently, the temperature-field simulations of the diffusive AAH model clearly demonstrate the presence of an extended-localized transition.

We extract the temperature evolutions to delve deeper into the quantitative analysis of the thermal behavior within the extended-localized transition. Firstly, we extract the maximum temperature of the 17th ring. This is the localization ring of the slowest-decaying branch for the localized state. For a comparative analysis, we also extract the maximum temperature of the 12th ring, which is the localization ring of the ninth-slowest-decaying branch for the localized state. The distribution of uniform excitation

is close to that of the extended state. So for the diffusive extended state, the simulated (theoretical) maximum-temperature evolutions of both rings correspond with each other and are predicted by the decay rate of the simulated (theoretical) slowest-decaying branch, as shown in Fig. 3(c). The theoretical results obtained by our solving the thermal-coupling equations (see Appendix C) slightly deviate from the simulated results due to the slight difference between the theoretical tight-binding model and the simulated structure. On the other hand, the uniform excitation can be approximately considered as the superposition of all localized-state distributions. So for the localized state, the temperature evolution of each ring is close to the reference line predicted by its corresponding localized branch, which is evident in Fig. 3(d). Besides, the temperature evolutions of the 17th and 12th rings decay slightly more slowly than the reference lines of the slowest-decaying and ninth-slowest-decaying branches. The reason is that the maximum-temperature decay of

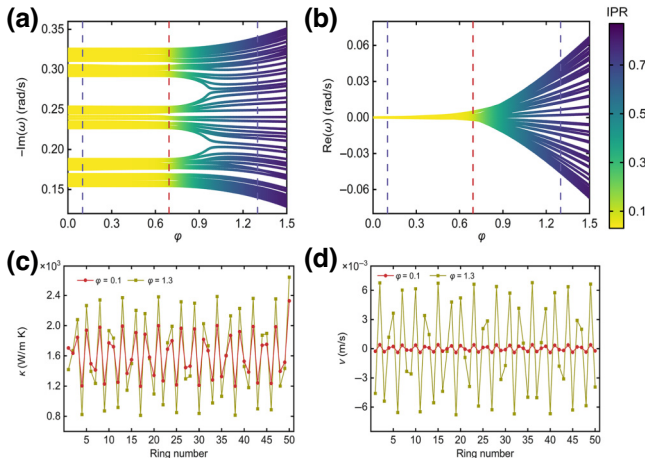


FIG. 5. Diffusive APT symmetric AAH model. (a) Decay rates and (b) eigenfrequencies with different imaginary phases. The color bar indicates the IPR. The dashed red line marks the extended-localized (APT unbroken-broken) transition point  $\phi = \ln(2h/V) = \ln(2) \approx 0.693$ . Adjusted (c) thermal conductivities and (d) rotation velocities of each ring for the extended state ( $\phi = 0.1$ ) and the localized state ( $\phi = 1.3$ ), which are marked as dashed purple lines in (a),(b). Here we set  $V = h$ . Other parameters are the same as in Fig. 2.

both rings is slowed down by their adjacent rings, which also have a high-temperature region under the uniform initial excitation. Furthermore, the maximum temperature of the 17th ring decays more slowly than the maximum temperature of the 12th ring because of the decay-rate difference between the slowest-decaying branch and the ninth-slowest-decaying branch.

The temperature field alone can only tell us the degree of localization qualitatively. To quantitatively characterize the localization of the temperature field, we should use the temperature IPR (TIPR), which is the thermal analogue of the IPR in condensed-matter physics. The TIPR is defined as

$$\rho_{\text{TIPR}} = \frac{\sum_j (T_{j,\max} - T_{j,\min})^4}{\left(\sum_j (T_{j,\max} - T_{j,\min})^2\right)^2}, \quad (6)$$

where  $T_{j,\max}$  and  $T_{j,\min}$  are the maximum and minimum temperatures of the  $j$  th ring. Similarly to the IPR, the TIPR approaches zero for the extended state and becomes large for the localized state. The TIPR for the diffusive AAH model ( $N = 50$ ) is shown in Fig. 3(e). With the increase of strength of the quasiperiodic potential, the TIPR also increases similarly as the IPR. However, for the localized state, the TIPR is evidently smaller than the IPR [see Fig. 2(a)]. The reason is that the decay rates of several branches are close to the decay rate of the slowest-decaying branch, so in the temperature field

these branches will also emerge in addition to the slowest-decaying branch, which will reduce the TIPR.

Next we discuss the size effect in temperature-field simulations for the diffusive AAH model according to the TIPR. Figure 3(f) presents the phase diagram of the TIPR with different numbers of rings  $N$  and strengths of the quasiperiodic potential  $V$ . Besides, we extract the TIPR with different numbers of rings  $N$  for the extended state, the transition point, and the localized state, as demonstrated in Fig. 3(g). When  $V$  is unchanged, the TIPR exhibits a decreasing trend with increasing  $N$ . This phenomenon can be attributed to more branches with a decay rate close to decay rate of the slowest-decaying branch when  $N$  increases, which will reduce the TIPR.

## V. TEMPERATURE-FIELD SIMULATIONS OF THE DIFFUSIVE AAH MODEL UNDER LOCAL EXCITATION

We proceed by altering the initial condition to local excitation (see Appendix B). As depicted in Fig. 4(a), the temperature field for the extended state is uniformly distributed among different localization centers. In contrast, for the localized state, as evident in Fig. 4(b), the temperature field remains confined within multiple localization centers. As before, we extract the maximum-temperature evolutions of the 17th and 12th rings. For the extended state, the maximum-temperature evolutions for both rings largely deviate from the reference lines predicted by the slowest-decaying branch under local excitation, which is demonstrated in Fig. 4(c). The reason is that the local excitation does not conform to the eigenstate distribution of the extended state, so the temperature evolution will not follow the decay rate of the slowest-decaying branch. Nevertheless, for the localized state, as the eigenstate distributions align more closely with the initial condition, the temperature evolutions for both rings deviate less from the reference lines predicted by their respective branches [see Fig. 4(d)] than the ones for the extended state. In contrast to the uniform-excitation case, the temperature evolution for both rings decays slightly faster than their respective branches because the initial temperature field of their adjacent rings is at thermal equilibrium under local excitation. With different initial conditions, the TIPR with local excitation [as depicted in Fig. 4(e)] is slightly larger than the TIPR with uniform excitation [see Fig. 3(e)]. The phase diagram of the TIPR with different numbers of rings  $N$  and strengths of the quasiperiodic potential  $V$  is shown in Fig. 4(f). We also extract the TIPR with different numbers of rings  $N$  for the extended state, the transition point, and the localized state, as demonstrated in Fig. 4(g). The results for the size effect under local excitation are similar to the results under uniform excitation. Furthermore, we report the temperature-field simulations for gradient and random initial excitations in

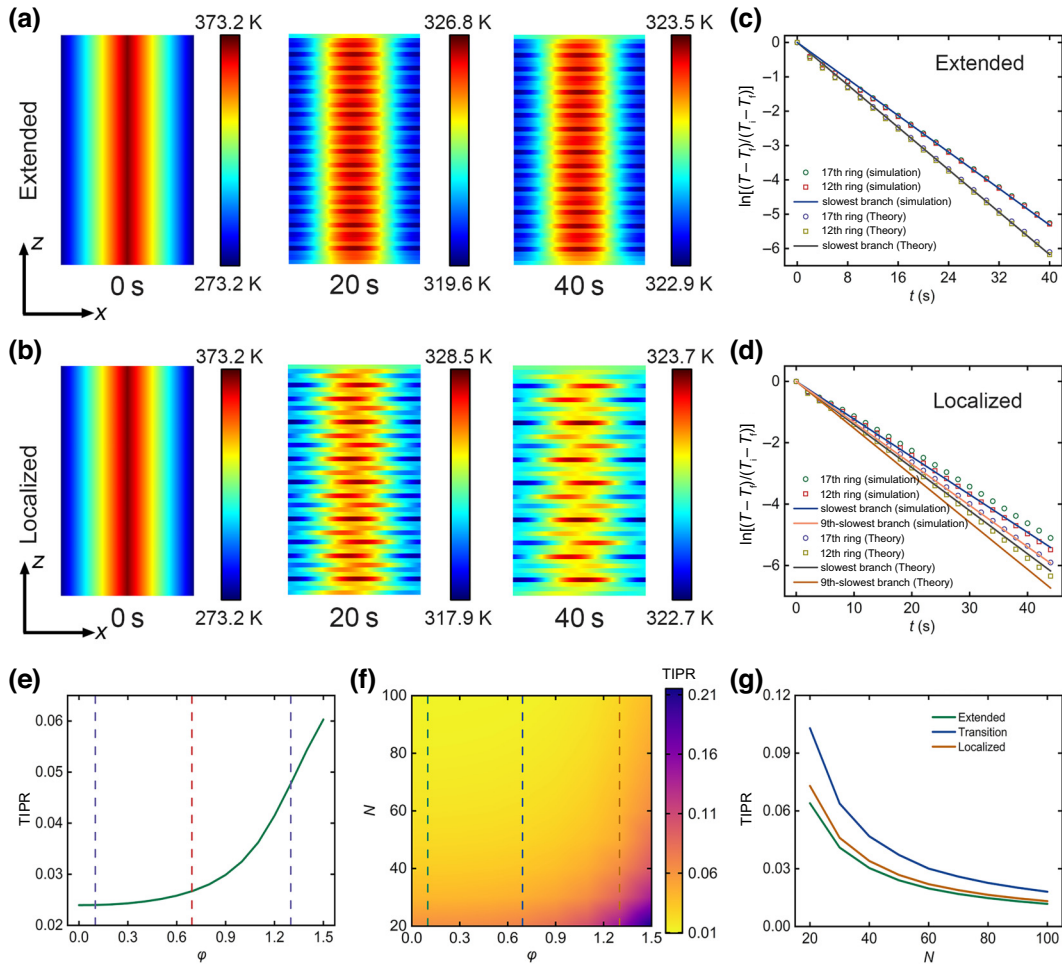


FIG. 6. Temperature-field simulations for the diffusive APT symmetric AAH model. (a) Extended state ( $\varphi = 0.1$ ) and (b) localized state ( $\varphi = 1.3$ ). (c) Simulated and theoretical normalized maximum-temperature evolutions of the 17th and 12th rings for the extended state. (d) Simulated and theoretical normalized maximum-temperature evolutions of the 17th and 12th rings for the localized state. (e) TIPR with different imaginary phases. (f) Phase diagram of the TIPR with different numbers of rings  $N$  and imaginary phase  $\varphi$ . (g) TIPR with different numbers of rings for the extended state, the transition point, and the localized state, which are marked as dashed lines in (f). The parameters are the same as in Fig. 3.

Appendix D, which shows the universality of the extended-localized transition under more initial conditions. We also report temperature-field simulations for the case of  $V = 0$  in Appendix E. The temperature field for a periodic system shows a very uniform distribution under different excitations [see Fig. 10], which verifies that the quasidisorder of parameters is the key to the phenomenon of multiple localization centers.

## VI. DIFFUSIVE APT SYMMETRIC AAH MODEL AND ITS TEMPERATURE-FIELD SIMULATIONS

Next we introduce an imaginary phase to implement the diffusive APT symmetric AAH model. Similarly to the derivation of the diffusive AAH Hamiltonian, the diffusive

APT symmetric AAH Hamiltonian can be expressed as

$$\hat{H} = i \sum_j \left[ h \hat{c}_{j+1}^\dagger \hat{c}_j + h \hat{c}_j^\dagger \hat{c}_{j+1} - (V \cos(2\pi\alpha j + i\varphi) + Mh) \hat{c}_j^\dagger \hat{c}_j \right], \quad (7)$$

where  $\varphi$  represents the imaginary phase. The extended-localized transition occurs at the APT transition point  $\varphi_c = \ln(2h/V)$  [14]. This exotic property has been numerically verified through the decay rates and eigenfrequencies of the diffusive APT symmetric AAH model, as shown in Figs. 5(a) and 5(b). From the spectrum we find that the extended state is in the APT unbroken phase, while the localized state is in the APT broken phase.

Furthermore, the topological properties of the diffusive APT symmetric AAH model can be characterized by a

winding number [14]. By introducing a real phase  $\phi$  into the on-site potential, we can express the Hamiltonian as

$$\hat{H}(\phi) = i \sum_j \left[ h \hat{c}_{j+1}^\dagger \hat{c}_j + h \hat{c}_j^\dagger \hat{c}_{j+1} - (V \cos(2\pi\alpha j + \phi + i\varphi) + Mh) \hat{c}_j^\dagger \hat{c}_j \right]. \quad (8)$$

The winding number  $v_\phi$  can be defined as

$$v_\phi = \frac{i}{2\pi N} \int_0^{2\pi} d\phi \partial_\phi \ln \det [\hat{H}(\phi) - E_B], \quad (9)$$

where  $E_B$  is the base energy. For the extended state,  $v_\phi = 0$ . In contrast, for the localized state,  $v_\phi = -1$  when  $\varphi > 0$  and  $v_\phi = 1$  when  $\varphi < 0$ .

For the diffusive APT symmetric AAH model with a complex on-site potential, the rotation terms of the rings should be introduced and adjusted, in addition to their thermal conductivities. By establishing a mapping between the diffusive APT symmetric AAH model and the ring chain's Hamiltonian, we obtain the following relations:

$$\begin{aligned} S_1 + i\beta v_1 &= -(V \cos(2\pi\alpha + i\varphi) + Mh), \\ S_j + i\beta v_j &= -(V \cos(2\pi\alpha j + i\varphi) + Mh), \\ S_N + i\beta v_N &= -(V \cos(2\pi\alpha N + i\varphi) + Mh), \end{aligned} \quad (10)$$

where  $j = 2, \dots, N-1$ . Note that the real part of the on-site potential corresponds to the on-site term of each ring, while the imaginary part corresponds to the rotation term. The solution of Eq. (10) provides the adjusted thermal conductivities and rotation velocities of the rings. To illustrate this point, we consider an extended state ( $\varphi = 0.1$ ) and a localized state ( $\varphi = 1.3$ ) as two examples. The distributions of the adjusted thermal conductivities and rotation velocities for these states are presented in Figs. 5(c) and 5(d).

Next we perform temperature-field simulations for the diffusive APT symmetric AAH model under uniform excitation. For the extended state ( $\varphi = 0.1$ ) [see Fig. 6(a)], the temperature field demonstrates a uniform distribution and remains stationary. Conversely, for the localized state when  $\varphi = 1.3$ , the temperature distribution distinctly reveals moving multiple localization centers, as depicted in Fig. 6(b). This observation suggests a simultaneous occurrence of an extended-localized transition [represented by an increasing TIPR with  $\varphi$  in Fig. 6(e)] and an APT unbroken-broken transition for the diffusive APT symmetric AAH model. Additionally, we extract the maximum-temperature evolutions of the 17th and 12th rings. For the extended state, the evolutions of the maximum temperatures for both rings align with the reference lines predicted by the slowest-decaying branch, as shown in Fig. 6(c).

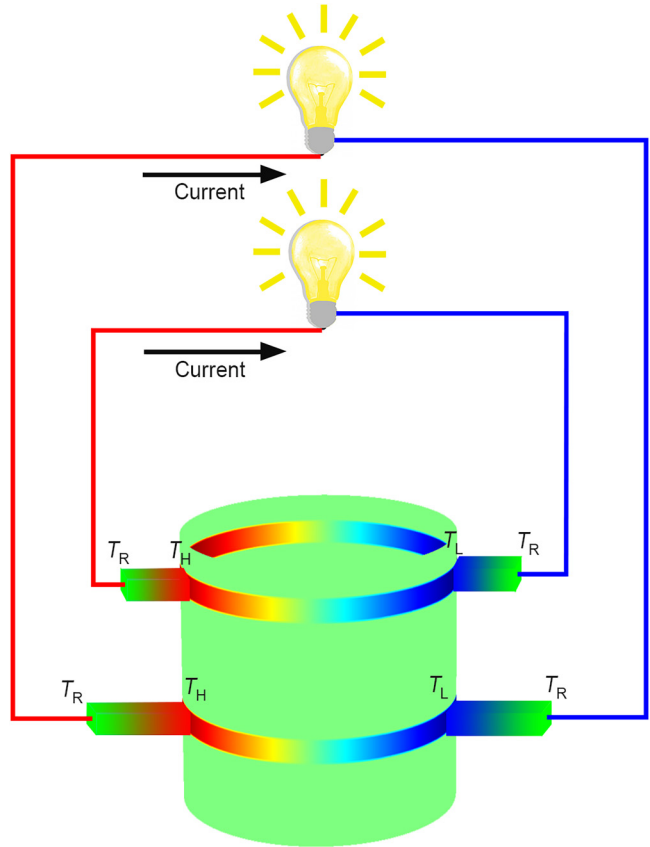


FIG. 7. Double-trace distributed generator. The cuboid indicates the thermoelectric material. The temperature at the hot source, the temperature at the cold source, and room temperature are denoted by  $T_H$ ,  $T_L$ , and  $T_R$ , respectively.

Meanwhile, for the localized state [see Fig. 6(d)], the maximum temperature of the 17th ring decays more slowly than the maximum temperature of the 12th ring because of the decay-rate difference between the slowest-decaying branch and ninth-slowest-decaying branch. Besides, the temperature evolutions of both rings decay slightly more slowly than the reference lines predicted by the corresponding branches. The phase diagram of the TIPR with different numbers of rings  $N$  and imaginary phases  $\varphi$  is shown in Fig. 6(f). We also extract the TIPR with different numbers of rings  $N$  for the extended state, the transition point, and the localized state, as demonstrated in Fig. 6(g). The results for the temperature evolution and size effect for the diffusive APT symmetric AAH model are similar to the results for the diffusive AAH model.

## VII. EXPERIMENTAL SUGGESTIONS

Now we provide some experimental suggestions for implementing the diffusive AAH model. The experimental setup proposed in Ref. [42] can be used to construct the coupled-ring chain structure. However, it is crucial to ensure that the parameters of the rings should conform to the results of our theoretical calculations. We suggest using

well-designed composite materials based on effective-medium theory to meet this requirement. For instance, adjusting the doping rates of materials with high contrast, such as copper and polydimethylsiloxane, can help achieve the necessary material parameters. Furthermore, advection can provide a reasonable degree of freedom for flexibly tuning the effective thermal conductivity [53,54].

### VIII. POTENTIAL APPLICATION: DOUBLE-TRACE DISTRIBUTED GENERATOR

We propose a potential application of double localization centers (multiple localization centers by extension naturally), referred to as the “double-trace distributed generator.” In a thermal system, high-temperature waste heat and low-temperature waste heat are often present. By connecting the two positions of a coupled-ring chain structure to high-temperature and low-temperature waste-heat sources and incorporating thermoelectric materials, one can generate external electricity. When the thermal system ceases to function, the high-temperature and low-temperature heat sources disappear, causing the temperature field of the structure to evolve and leading to the emergence of the phenomenon of double localization centers. As shown in Fig. 7, we can choose the positions of thermoelectric materials as where the double localization centers appear. By our doing so, the power and duration of the thermoelectric materials can be significantly increased in comparison with a structure without adjusted parameters, and two objects can be powered simultaneously. Our device has a straightforward structure and flexible distributed-power-generation capabilities when compared with traditional electric generators.

### IX. CONCLUSION

In this study, we successfully demonstrate the extended-localized transition within diffusion systems. This transition is realized through a diffusive quasicrystal constructed with use of a coupled-ring chain structure. By carefully adjusting the thermal conductivities of the rings, we establish the diffusive AAH model successfully. Through temperature-field simulations, we clearly confirm the extended-localized transition for the diffusive AAH model based on this ring-shaped chain. The temperature evolution and size effect of this transition are further studied quantitatively. Meanwhile, we use the initial condition of local excitation to investigate the temperature field of both the extended state and the localized state. Furthermore, we introduce non-Hermitian physics into the diffusive AAH model to investigate the extended-localized transition. This diffusive APT symmetric AAH model shows a phenomenon of moving multiple localization centers in the temperature-field simulations. Finally, we provide some experimental suggestions and propose a potential application. We anticipate that our findings will stimulate further

research into quasidisordered and disordered phases in diffusion systems [55,56]. For instance, the integer quantum Hall insulator in diffusion systems can be studied due to its mapping to the diffusive AAH model [57,58]. The coupled-ring chain structure can be used to realize various topological states in diffusion systems [59–61]. Besides, these exotic phases of matter can help in the design of innovative thermal materials for efficient and robust heat manipulation [62].

### ACKNOWLEDGMENTS

We are extremely grateful to Professor Ruibao Tao for his incredibly insightful discussions and guidance, and we also thank Dr. Xinchen Zhou for his valuable discussions. J.H. acknowledges the financial support provided by the National Natural Science Foundation of China under Grants No. 12035004 and No. 12320101004 and the Innovation Program of the Shanghai Municipal Education Commission under Grant No. 2023ZKZD06. Y.L. acknowledges the support by the National Natural Science Foundation of China under Grants No. 92163123 and No. 52250191 and Zhejiang Provincial Natural Science Foundation of China under Grant No. LZ24A050002.

### APPENDIX A: LYAPUNOV EXPONENT OF THE DIFFUSIVE AAH MODEL

Here we extract the Lyapunov exponent of diffusive AAH model. For the diffusive AAH model discussed in the main text, the extended-localized transition occurs at  $V = 2h$  due to the self-duality [4]. The model is in the extended phase when  $V < 2h$ , while it is in the localized phase if  $V > 2h$ . Furthermore, the localized eigenstate has an exponentially localized form with  $|\psi| = |\psi|_{\max} e^{-\eta|i - i_0|}$ , where  $i_0$  is the ring index of the localization center and  $\eta$  is the Lyapunov exponent [16]. The Lyapunov exponent, similarly to the IPR, also characterizes the degree of localization. However, it is difficult to extract the Lyapunov exponent from the temperature field. The reason is that several slowly decaying branches will emerge in the temperature field due to their close decay rates, as can be seen from Fig. 2(a). However, we can extract the Lyapunov exponent from the theoretical and simulated eigenstate distributions by exponential fitting. The results for the Lyapunov exponent of the slowest-decaying branch are shown in Fig. 8, where a clear extended-localized phase transition can be found.

### APPENDIX B: TEMPERATURE-FIELD SIMULATIONS UNDER UNIFORM AND LOCAL EXCITATIONS

We perform the temperature-field simulations with COMSOL MULTIPHYSICS. The ambient temperature is set to

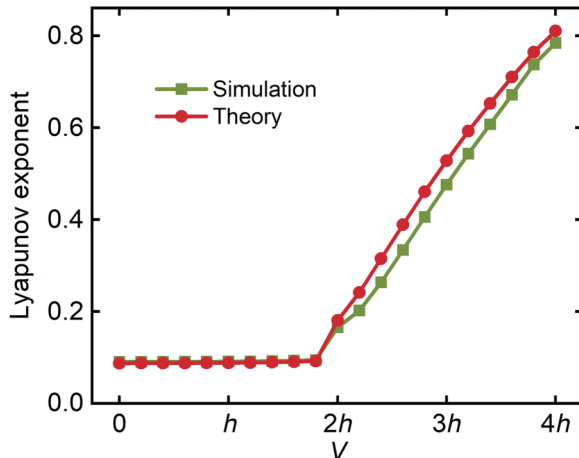


FIG. 8. Theoretical and simulated Lyapunov exponent of the slowest-decaying branch. The parameters are the same as in Fig. 2.

be 293.2 K. We stop the simulation when the difference between maximum and minimum temperatures of the structure drops below 0.5 K. We call the temperature field under this condition the “final state.” For uniform excitation, we set the initial temperature at the middle of the channel  $T_h$  as the highest and the initial temperature at the ends (periodic boundary condition)  $T_l$  as the lowest. The initial temperature field between these two positions is linearly distributed. In the case of local excitation, we stimulate  $N/5$  rings, which are the localization rings of  $N/5$  slowly decaying branches for the localized state. The temperatures of the remaining rings are set at the thermal equilibrium  $T_f = (T_h + T_l)/2$ . For the diffusive AAH model ( $N = 50$ ) discussed in the main text, these ten rings are ranked as follows: 17th (slowest), 38th (second slowest), 4th (3rd slowest), 30th (4th slowest), 25th (5th slowest), 9th (6th slowest), 46th (7th slowest), 43rd (8th slowest), 12th (9th slowest), and 22nd (10th slowest).

### APPENDIX C: THEORETICAL SOLUTION FOR THERMAL-COUPLING EQUATIONS

The detailed theoretical solution for the thermal-coupling equations involves our spatially discretizing the ring structure and then solving the partial differential equations. As shown in the main text, the temperature field  $T_j(x, t)$  of the  $j$  th ring is expressed in the thermal-coupling equation:

$$\begin{aligned} \frac{\partial T_j(x, t)}{\partial t} &= \frac{\kappa_j}{\rho_j C_j} \frac{\partial^2 T_j(x, t)}{\partial x^2} + v_j \frac{\partial T_j(x, t)}{\partial x} \\ &+ h_{j-1,j} [T_{j-1}(x, t) - T_j(x, t)] \\ &+ h_{j,j} [T_{j+1}(x, t) - T_j(x, t)], \end{aligned} \quad (C1)$$

Subsequently, we discretize each ring into  $M$  segments and designate the temperature field for each segment of the  $j$  th ring as  $T_{j,k}(t)$ , where  $j = 1, \dots, N$  and  $k = 1, \dots, M$ . Additionally, because of the circular structure, the condition  $T_{j,1}(t) = T_{j,M}(t)$  must be imposed. Hence, the discretized thermal-coupling equation of the  $j$  th ring can be expressed as

$$\begin{aligned} \frac{\partial T_{j,k}(t)}{\partial t} &= \frac{\kappa_j}{\rho_j C_j} \frac{T_{j,k+1}(t) + T_{j,k-1}(t) - 2T_{j,k}(t)}{a^2} \\ &+ v_j \frac{T_{j,k+1}(t) - T_{j,k-1}(t)}{2a} \\ &+ h_{j-1,j} [T_{j-1,k}(t) - T_{j,k}(t)] \\ &+ h_{j,j} [T_{j+1,k}(t) - T_{j,k}(t)], \end{aligned} \quad (C2)$$

where  $a = 2\pi R/M$ . Next we substitute the parameters of the diffusive AAH model and the initial conditions (uniform or local excitation) into the discretized thermal-coupling equations. Then we solve these equations numerically. After extracting the maximum temperature  $\max [T_{j,1}(t), \dots, T_{j,M}(t)]$  of the  $j$  th ring, we obtain the theoretical results depicted in Figs. 3(c), 3(d), 4(c), and 4(d).

### APPENDIX D: TEMPERATURE-FIELD SIMULATIONS OF THE DIFFUSIVE AAH MODEL UNDER GRADIENT AND RANDOM EXCITATIONS

In this appendix, we report temperature-field simulations under initial excitations other than uniform and local excitations. Firstly, we set the gradient condition to excite the temperature field. For gradient excitation, the temperature gradient for the central two rings has a maximum value and decreases with a gradient for the other rings, while the initial temperature field for the boundary rings reaches thermal equilibrium [see Figs. 9(a) and 9(b)]. The temperature field for the extended state concentrates at the center and has a distribution similar to the distribution with the initial condition [see Fig. 9(a)]. However, the temperature field for the localized state exhibits a phenomenon of multiple localization centers [see Fig. 9(b)]. Secondly, random excitation is applied to investigate the temperature-field behavior, which means that the initial temperature gradient for each ring is randomly imposed [see Figs. 9(c) and 9(d)]. As with the other excitations, the temperature field for the extended state is uniform [see Fig. 9(c)], while the temperature field for the localized state demonstrates several localization centers [see Fig. 9(d)]. Both gradient excitation and random excitation have demonstrated an obvious extended-localized transition in the temperature-field simulations.

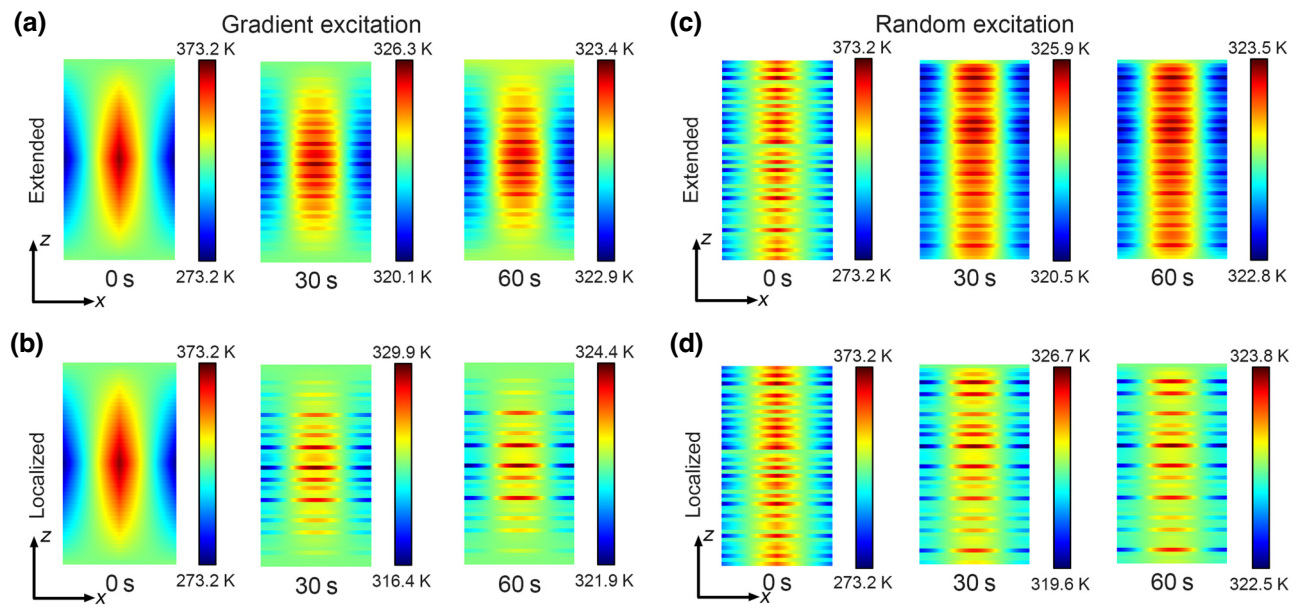


FIG. 9. Temperature-field simulations under gradient and random excitation. (a) Extended state ( $V = h$ ) and (b) localized state ( $V = 3h$ ) under gradient excitation. (c) Extended state ( $V = h$ ) and (d) localized state ( $V = 3h$ ) under random excitation. The parameters are the same as in Fig. 3.

#### APPENDIX E: TEMPERATURE-FIELD SIMULATIONS WITHOUT A QUASIPERIODIC ON-SITE POTENTIAL

In this appendix, we report temperature-field simulations of the diffusive AAH model with zero on-site potential ( $V = 0$ ). As shown in Fig. 10, we studied this

issue under four initial conditions: uniform, local, gradient, and random excitations. For the uniform and random excitations, the temperature field demonstrates a fully uniform distribution [see Figs. 10(a) and 10(d)]. For local excitation, the temperature field for  $V = 0$  [see Fig. 10(b)] is much more uniformly distributed among different localization centers than is the case for  $V = h$  and  $V = 3h$

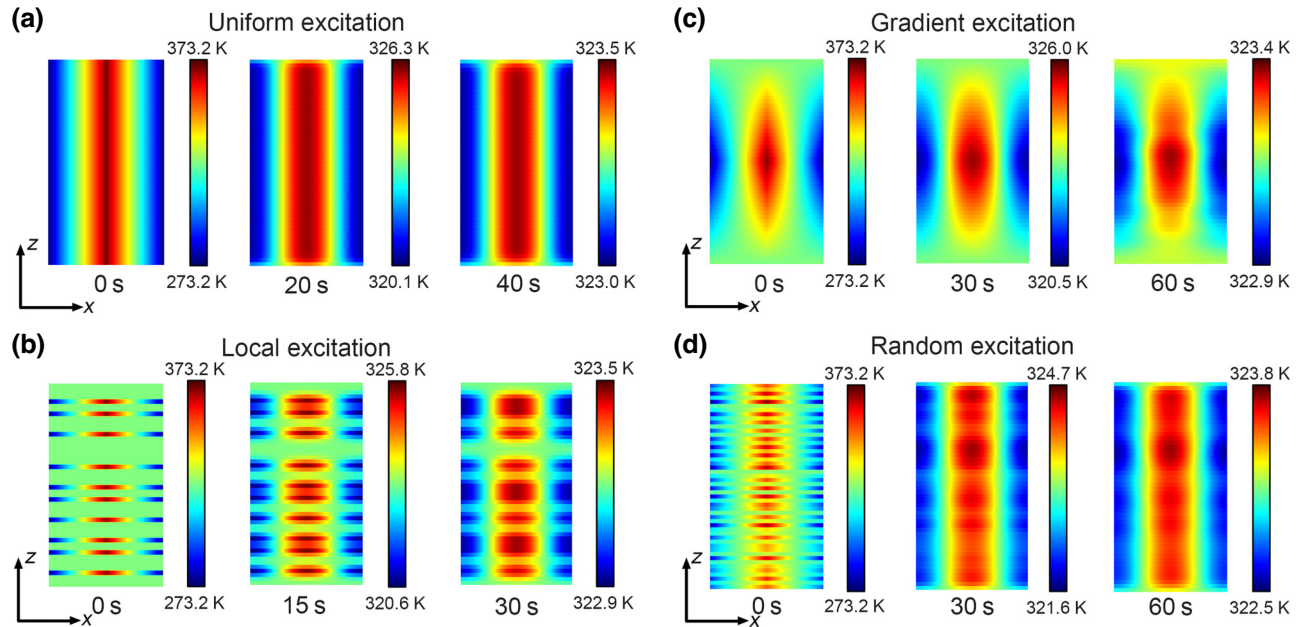


FIG. 10. Temperature-field simulations without quasiperiodicity: (a) uniform excitation, (b) local excitation, (c) gradient excitation, and (d) random excitation. The parameters are the same as in Fig. 3.

[see Figs. 4(a) and 4(b)]. For gradient excitation, the temperature field concentrates at the center and has a distribution similar to the distribution with the initial condition [see Fig. 10(c)]. The temperature fields for  $V = 0$  show a distribution totally different from that for  $V = 3h$  in the localized phase. So the phenomenon of multiple localization centers actually stems from the quasidisorder of the system.

- 
- [1] P. W. Anderson, Absence of diffusion in certain random lattices, *Phys. Rev.* **109**, 1492 (1958).
- [2] E. Abrahams, P. W. Anderson, D. C. Licciardello, and T. V. Ramakrishnan, Scaling theory of localization: Absence of quantum diffusion in two dimensions, *Phys. Rev. Lett.* **42**, 673 (1979).
- [3] P. A. Lee and T. V. Ramakrishnan, Disordered electronic systems, *Rev. Mod. Phys.* **57**, 287 (1985).
- [4] S. Aubry and G. André, Analyticity breaking and Anderson localization in incommensurate lattices, *Ann. Isr. Phys. Soc.* **3**, 133 (1980).
- [5] P. G. Harper, Single band motion of conduction electrons in a uniform magnetic field, *Proc. Phys. Soc. London Sect. A* **68**, 874 (1955).
- [6] G. Roati, C. D'Errico, L. Fallani, M. Fattori, C. Fort, M. Zaccanti, G. Modugno, M. Modugno, and M. Inguscio, Anderson localization of a non-interacting Bose-Einstein condensate, *Nature* **453**, 895 (2008).
- [7] Y. Wang, J.-H. Zhang, Y. Li, J. Wu, W. Liu, F. Mei, Y. Hu, L. Xiao, J. Ma, C. Chin, and S. Jia, Observation of interaction-induced mobility edge in an atomic Aubry-André wire, *Phys. Rev. Lett.* **129**, 103401 (2022).
- [8] Q. Lin, T. Li, L. Xiao, K. Wang, W. Yi, and P. Xue, Topological phase transitions and mobility edges in non-Hermitian quasicrystals, *Phys. Rev. Lett.* **129**, 113601 (2022).
- [9] Y. Lahini, R. Pugatch, F. Pozzi, M. Sorel, R. Morandotti, N. Davidson, and Y. Silberberg, Direct observation of a localization transition in quasiperiodic photonic lattices, *Phys. Rev. Lett.* **103**, 013901 (2009).
- [10] M. Verbin, O. Zilberberg, Y. E. Kraus, Y. Lahini, and Y. Silberberg, Observation of topological phase transitions in photonic quasicrystals, *Phys. Rev. Lett.* **110**, 076403 (2013).
- [11] W. Zhang, H. Wang, H. Sun, and X. Zhang, Non-Abelian inverse Anderson transitions, *Phys. Rev. Lett.* **130**, 206401 (2023).
- [12] H. Wang, W. Zhang, H. Sun, and X. Zhang, Observation of non-Abelian Anderson localization and transition in topoelectrical circuits, *Phys. Rev. B* **108**, 144203 (2023).
- [13] Q. Zeng, S. Chen, and R. Lü, Anderson localization in the non-Hermitian Aubry-André-Harper model with physical gain and loss, *Phys. Rev. A* **95**, 062118 (2017).
- [14] S. Longhi, Topological phase transition in non-Hermitian quasicrystals, *Phys. Rev. Lett.* **122**, 237601 (2019).
- [15] S. Longhi, Metal-insulator phase transition in a non-Hermitian Aubry-André-Harper model, *Phys. Rev. B* **100**, 125157 (2019).
- [16] H. Jiang, L. Lang, C. Yang, S.-L. Zhu, and S. Chen, Interplay of non-Hermitian skin effects and Anderson localization in non-reciprocal quasicrystals, *Phys. Rev. B* **100**, 054301 (2019).
- [17] Y. Liu, Y. Wang, X.-J. Liu, Q. Zhou, and S. Chen, Exact mobility edges, *PT*-symmetry breaking and skin effect in one-dimensional non-Hermitian quasicrystals, *Phys. Rev. B* **103**, 014203 (2021).
- [18] Y. Liu, Q. Zhou, and S. Chen, Localization transition, spectrum structure and winding numbers for one-dimensional non-Hermitian quasicrystals, *Phys. Rev. B* **104**, 024201 (2021).
- [19] S. Yang, J. Wang, G. Dai, F. Yang, and J. Huang, Controlling macroscopic heat transfer with thermal metamaterials: Theory, experiment and application, *Phys. Rep.* **908**, 1 (2021).
- [20] Y. Li, W. Li, T. Han, X. Zheng, J. Li, B. Li, S. Fan, and C.-W. Qiu, Transforming heat transfer with thermal metamaterials and devices, *Nat. Rev. Mater.* **6**, 488 (2021).
- [21] Z. Zhang, L. Xu, T. Qu, M. Lei, Z.-K. Lin, X. Ouyang, J.-H. Jiang, and J. Huang, Diffusion metamaterials, *Nat. Rev. Phys.* **5**, 218 (2023).
- [22] F. Yang, Z. Zhang, L. Xu, Z. Liu, P. Jin, P. Zhuang, M. Lei, J. Liu, J.-H. Jiang, X. Ouyang, F. Marchesoni, and J. Huang, Controlling mass and energy diffusion with metamaterials, *Rev. Mod. Phys.* **96**, 015002 (2024).
- [23] R. Ju, G. Xu, L. Xu, M. Qi, D. Wang, P.-C. Cao, R. Xi, Y. Shou, H. Chen, C.-W. Qiu, and Y. Li, Convective thermal metamaterials: Exploring high-efficiency, directional, and wave-like heat transfer, *Adv. Mater.* **35**, 2209123 (2022).
- [24] C. Fan, Y. Gao, and J. Huang, Shaped graded materials with an apparent negative thermal conductivity, *Appl. Phys. Lett.* **92**, 251907 (2008).
- [25] T. Chen, C.-N. Weng, and J.-S. Chen, Cloak for curvilinearly anisotropic media in conduction, *Appl. Phys. Lett.* **93**, 114103 (2008).
- [26] Y. Gao and J. Huang, Unconventional thermal cloak hiding an object outside the cloak, *EPL* **104**, 44001 (2013).
- [27] R. Wang, L. Xu, Q. Ji, and J. Huang, A thermal theory for unifying and designing transparency, concentrating and cloaking, *J. Appl. Phys.* **123**, 115117 (2018).
- [28] P. Jin, J. Liu, L. Xu, J. Wang, X. Ouyang, J.-H. Jiang, and J. Huang, Tunable liquid-solid hybrid thermal metamaterials with a topology transition, *Proc. Natl. Acad. Sci. USA* **120**, e2217068120 (2023).
- [29] N. Zhu, X. Shen, and J. Huang, Converting the patterns of local heat flux via thermal illusion device, *AIP Adv.* **5**, 053401 (2015).
- [30] L. Xu, R. Wang, and J. Huang, Camouflage thermotics: A cavity without disturbing heat signatures outside, *J. Appl. Phys.* **123**, 245111 (2018).
- [31] R. Hu, S. Zhou, Y. Li, D.-Y. Lei, X. Luo, and C.-W. Qiu, Illusion thermotics, *Adv. Mater.* **30**, 1707237 (2018).
- [32] R. Hu, S. Huang, M. Wang, X. Luo, J. Shiomi, and C.-W. Qiu, Encrypted thermal printing with regionalization transformation, *Adv. Mater.* **31**, 1807849 (2019).
- [33] F. Yang, L. Xu, and J. Huang, Thermal illusion of porous media with convection-diffusion process: Transparency, concentrating, and cloaking, *ES Energy Environ.* **6**, 45 (2019).

- [34] P. Jin, J. Liu, F. Yang, F. Marchesoni, J.-H. Jiang, and J. Huang, In situ simulation of thermal reality, *Research* **6**, 0222 (2023).
- [35] L. Xu, S. Yang, and J. Huang, Passive metashells with adaptive thermal conductivities: Chameleonlike behavior and its origin, *Phys. Rev. Appl.* **11**, 054071 (2019).
- [36] F. Yang, B. Tian, L. Xu, and J. Huang, Experimental demonstration of thermal chameleonlike rotators with transformation-invariant metamaterials, *Phys. Rev. Appl.* **14**, 054024 (2020).
- [37] Z. Liu, Chapter 8 in *Diffusionics: Diffusion Process Controlled by Diffusion Metamaterials*, edited by F.-B. Yang and J.-P. Huang (Springer, Singapore, 2024).
- [38] Y. Li, Y.-G. Peng, L. Han, M.-A. Miri, W. Li, M. Xiao, X.-F. Zhu, J. Zhao, A. Alù, S. Fan, and C.-W. Qiu, Antiparity-time symmetry in diffusive systems, *Science* **364**, 170 (2019).
- [39] G. Xu, Y. Li, W. Li, S. Fan, and C.-W. Qiu, Configurable phase transitions in a topological thermal material, *Phys. Rev. Lett.* **127**, 105901 (2021).
- [40] P.-C. Cao, R. Ju, D. Wang, M. Qi, Y.-K. Liu, Y.-G. Peng, H. Chen, X.-F. Zhu, and Y. Li, Observation of parity-time symmetry in diffusive systems, *Sci. Adv.* **15**, 2169 (2024).
- [41] G. Xu, W. Li, X. Zhou, H. Li, Y. Li, S. Fan, S. Zhang, D. N. Christodoulides, and C.-W. Qiu, Observation of Weyl exceptional rings in thermal diffusion, *Proc. Natl. Acad. Sci. USA* **119**, e2110018119 (2022).
- [42] G. Xu, Y. Yang, X. Zhou, H. Chen, A. Alù, and C.-W. Qiu, Diffusive topological transport in spatiotemporal thermal lattices, *Nat. Phys.* **18**, 450 (2022).
- [43] T. Yoshida and Y. Hatsugai, Bulk-edge correspondence of classical diffusion phenomena, *Sci. Rep.* **11**, 888 (2021).
- [44] M. Qi, D. Wang, P.-C. Cao, X.-F. Zhu, C.-W. Qiu, H. Chen, and Y. Li, Geometric phase and localized heat diffusion, *Adv. Mater.* **34**, 2202241 (2022).
- [45] H. Hu, S. Han, Y. Yang, D. Liu, H. Xue, G.-G. Liu, Z. Cheng, Q. Wang, S. Zhang, B. Zhang, and Y. Luo, Observation of topological edge states in thermal diffusion, *Adv. Mater.* **34**, 2202257 (2022).
- [46] Z. Liu, P.-C. Cao, L. Xu, G. Xu, Y. Li, and J. Huang, Higher-order topological in-bulk corner state in pure diffusion systems, *Phys. Rev. Lett.* **132**, 176302 (2024).
- [47] G. Xu, X. Zhou, S. Yang, J. Wu, and C.-W. Qiu, Observation of bulk quadrupole in topological heat transport, *Nat. Commun.* **14**, 3252 (2023).
- [48] H. Wu, H. Hu, X. Wang, Z. Xu, B. Zhang, Q. Wang, Y. Zheng, J. Zhang, T. Cui, and Y. Luo, Higher-order topological states in thermal diffusion, *Adv. Mater.* **35**, 202210825 (2023).
- [49] P.-C. Cao, Y. Li, Y.-G. Peng, M. Qi, W.-X. Huang, P.-Q. Li, and X.-F. Zhu, Diffusive skin effect and topological heat funneling, *Commun. Phys.* **4**, 230 (2021).
- [50] P.-C. Cao, Y.-G. Peng, Y. Li, and X.-F. Zhu, Phase-locking diffusive skin effect, *Chin. Phys. Lett.* **39**, 057801 (2022).
- [51] Q.-K.-L. Huang, Y.-K. Liu, P.-C. Cao, X.-F. Zhu, and Y. Li, Two-dimensional thermal regulation based on non-Hermitian skin effect, *Chin. Phys. Lett.* **40**, 106601 (2023).
- [52] Y.-K. Liu, P.-C. Cao, M. Qi, Q.-K.-L. Huang, F. Gao, Y.-G. Peng, Y. Li, and X.-F. Zhu, Observation of non-Hermitian skin effect in thermal diffusion, *Sci. Bull.* **69**, 1228 (2024).
- [53] Y. Li, K.-J. Zhu, Y.-G. Peng, W. Li, T. Yang, H.-X. Xu, H. Chen, X.-F. Zhu, S. Fan, and C.-W. Qiu, Thermal meta-device in analogue of zero-index photonics, *Nat. Mater.* **18**, 48 (2019).
- [54] G. Xu, K. Dong, Y. Li, H. Li, K. Liu, L. Li, J. Wu, and C.-W. Qiu, Tunable analog thermal material, *Nat. Commun.* **11**, 6028 (2020).
- [55] S. Tian, T. Wu, S. Hu, D. Ma, and L. Zhang, Boosting phonon transport across AlN/SiC interface by fast annealing amorphous layers, *Appl. Phys. Lett.* **124**, 042202 (2024).
- [56] Z. Liu and J. Huang, *Chin. Phys. Lett.* **40**, 110305 (2023).
- [57] L.-J. Lang, X. Cai, and S. Chen, Edge states and topological phases in one-dimensional optical superlattices, *Phys. Rev. Lett.* **108**, 220401 (2012).
- [58] Y. Kraus, Y. Lahini, Z. Ringel, M. Verbin, and O. Zilberberg, Topological states and adiabatic pumping in quasicrystals, *Phys. Rev. Lett.* **109**, 106402 (2012).
- [59] J. Cao, A. V. Kavokin, and A. V. Nalitov, Tamm states and gap topological numbers in photonic crystals, *Prog. Electromagn. Res.* **173**, 141 (2022).
- [60] J. Zheng, Z. Guo, Y. Sun, H. Jiang, Y. Li, and H. Chen, Topological edge modes in one-dimensional photonic artificial structures, *Prog. Electromagn. Res.* **177**, 1 (2023).
- [61] Y.-Z. Li, Z. Zhang, H. Chen, and F. Gao, Polarization-wavelength locked plasmonic topological states, *Prog. Electromagn. Res.* **178**, 37 (2023).
- [62] X. Zhou, X. Xu, and J. Huang, Adaptive multi-temperature control for transport and storage containers enabled by phase-change materials, *Nat. Commun.* **14**, 5449 (2023).